

Article

Evaluation of Ride Comfort under Vortex-Induced Vibration of Long-Span Bridge

Yafei Wang¹, Changfa Zhou^{2,3,4}, Jiwei Zhong¹, Zhengxing Wang¹, Wenfan Yao¹, Yuyin Jiang¹
and Shujin Laima^{1,2,3,4,*}

¹ National Key Laboratory of Bridge Intelligent and Green Construction, Wuhan 430034, China; wangyafei@foxmail.com (Y.W.); jw_zhong@sohu.com (J.Z.); wzx2332@126.com (Z.W.); justonevan@163.com (W.Y.); jiangyuyinjy@163.com (Y.J.)

² Key Laboratory of Smart Prevention and Mitigation of Civil Engineering Disasters of the Ministry of Industry and Information Technology, Harbin Institute of Technology, Harbin 150090, China; 17851145875@163.com

³ Key Laboratory of Structures Dynamic Behavior and Control of the Ministry of Education, Harbin Institute of Technology, Harbin 150090, China

⁴ School of Civil Engineering, Harbin Institute of Technology, Harbin 150090, China

* Correspondence: laimashujin@hit.edu.cn; Tel.: +86-451-8628-2068

Abstract: The increasing number of suspension bridges has led to designs favoring greater length and flexibility, resulting in a common problem of vortex-induced vibration. While vortex-induced vibration typically does not cause structural damage, it diminishes the bridge's fatigue resistance and has a detrimental impact on ride comfort. Additionally, this study introduces a road–bridge–vehicle vibration model, proposing an evaluation method for assessing ride comfort during vortex-induced vibrations in long-span bridges. This method features simplified modeling and swift calculations, circumventing the need for intricate finite element modeling and iterative solving. Furthermore, it evaluates ride comfort for vehicles crossing a prototype long-span suspension bridge using the Overall Vibration Total Value (OVTV) and Motion Sickness Incidence (MSI) criteria. This study also analyzes the influence of various parameters on OVTV and MSI, including vehicle speed, road grade, vortex-induced vibration frequency, and amplitude. It establishes a reference limit for vortex-induced vibration amplitude based on OVTV and MSI values. Moreover, the study substantiates that, within the context of vortex-induced vibration, the MSI value is more suitable for evaluating driving comfort compared to the OVTV.

Keywords: long-span bridge; vortex-induced vibration; ride comfort; motion sickness



Citation: Wang, Y.; Zhou, C.; Zhong, J.; Wang, Z.; Yao, W.; Jiang, Y.; Laima, S. Evaluation of Ride Comfort under Vortex-Induced Vibration of Long-Span Bridge. *Appl. Sci.* **2023**, *13*, 11505. <https://doi.org/10.3390/app132011505>

Academic Editor: José Neves

Received: 14 September 2023

Revised: 9 October 2023

Accepted: 18 October 2023

Published: 20 October 2023



Copyright: © 2023 by the authors. Licensee MDPI, Basel, Switzerland. This article is an open access article distributed under the terms and conditions of the Creative Commons Attribution (CC BY) license (<https://creativecommons.org/licenses/by/4.0/>).

1. Introduction

To reduce transportation costs, minimize spatial–temporal distances between regions, and align with the trends of regional integration and economic globalization, countries are actively constructing and enhancing transportation networks through infrastructure development. As the integral components of infrastructures, including high-speed railways and sea-crossing channels, long-span bridges have been widely constructed and applied all over the world, creating new span records [1]. Wind-induced vibrations, such as flutter, galloping, buffeting, and vortex-induced vibration, present significant challenges to the stability of long-span bridges. Among these vibration types, vortex-induced vibration is the most prevalent, occurring in numerous bridges both domestically and internationally [2–6]. Vortex-excited vibration is a wind-induced, self-excited vibration that typically manifests at low wind speeds on long-span bridges, and it is theoretically inevitable. Contrary to divergent vibrations like flutter and galloping, VIV rarely causes dynamic instability or catastrophic bridge damage. However, its relatively high amplitude, coupled with frequent occurrences, can inevitably reduce the structural strength and fatigue resistance of bridges [7–9], impacting visual safety and ride comfort.

In 2020, significant vortex vibrations with amplitudes ranging from 0.1 m to 0.3 m were observed on the Humen suspension bridge in China [10]. Other examples of VIV occurrences on real bridges include the Xihoumen Bridge [6] and Yingwuzhou Yangtze River Bridge [11] in China, as well as the Yi Sun-sin Bridge in Korea [12]. Investigations revealed that, despite the short duration of these conditions, several drivers experienced different levels of short-term physical discomfort [13]. The occurrence of vortex vibrations on the Humen Bridge led to panic among the on-site personnel and drivers, posing a significant traffic safety hazard. As a result, the bridge had to be closed for up to ten days, resulting in significant economic losses and public outcry [10].

Despite its limited amplitude, VIV can contribute to vehicle vibrations, causing short-term discomfort during extended driving. Concurrently, the literature shows that long-term high-intensity whole-body vibrations increase health risks, particularly to the lumbar spine and related nervous systems, as outlined in ISO 2631 [14]. Vehicle ride comfort remains a global research focus. Most studies concentrate on drivers' and passengers' comfort with respect to vibrations in everyday wind conditions, while also accounting for road irregularities and crosswinds. Zhang et al. [15] proposed a comprehensive evaluation method for vehicle ride comfort and driving safety on a slender coastal bridge under the influence of vehicle, wind, and wave loads, which evaluates ride comfort using the Overall Vibration Total Value (OVTV) index recommended by the ISO 2631-1 standard [14] and analyze driving safety based on roll safety criteria (RSC) and sideslip safety criteria (SSC). Nguyen et al. [16] assessed the ride comfort of vehicles travelling on a slender arch bridge, which is made of ultra-high performance fiber-reinforced concrete (UHPFRC) and under turbulent crosswinds; the results showed that the bridge's vibration response is significantly affected by crosswinds in terms of peak acceleration and frequency distribution. Camara et al. [17] investigated the comfort of drivers and passengers considering the road surface roughness and crosswind; the results showed that both road surface roughness and wind load have a significant impact on the comfort of drivers and passengers. Zhou et al. [18] numerically evaluated the ride comfort of three representative vehicles and assessed the impact of dynamic interaction between the bridge and the vehicle on ride comfort, considering typical traffic flow and wind excitation on a prototype of a long-span bridge. Montenegro et al. [19] analyzed the influence of vibration inside the train on ride comfort when the train passed a railway bridge under crosswind conditions, taking into account factors such as wind load, track conditions, speed, and the lateral vibration of the bridge, using the average and continuous comfort index in the European standard EN12299 [20] and the Sperling index in the Chinese standard GB/T5599-2019 [21] for evaluation and comparing the difference between the two standards. Bao et al. [22] developed a dynamic system for wind-suspended monorail bridges. They introduced a method for accurately simulating aerodynamic wind forces on both the bridge and moving vehicles. Additionally, they investigated how turbulent crosswinds impact the bridge's dynamic response and passenger comfort during vehicle travel. The findings indicate that turbulent crosswinds significantly affect the dynamic performance of the suspended monorail axle system. Passengers may experience discomfort when the vehicle traverses the bridge during strong turbulent crosswinds. Ribeiro et al. [23] assessed the dynamic performance of a steel arch bridge in Portugal under light rail traffic loads. They employed moving load models and vehicle-bridge interaction models to evaluate not only traffic safety but also passenger and pedestrian comfort.

However, few studies have considered the impact of whole-body vibrations on drivers and passengers under vortex-induced vibration. Yu et al. [24] devised a wind-vehicle-bridge coupling system tailored for assessing ride comfort during vortex-induced vibration, employing the ISO 2631-1:1997 standard [14]. Their findings suggest that as the number of vehicles on the bridge increases, the consideration of additional mass and damping from the vehicle-axle system leads to a reduction in the dynamic response OVTV of the vehicles. Concurrently, the study investigates how ride comfort is affected by factors such as vehicle speed, vehicle type, road roughness, and the number of vehicles. Zhu et al. [25], following

ISO 2631-1 [14] guidelines, introduced a comfort evaluation program for long-span bridges exposed to traffic flow during vortex-induced vibration. The wind–vehicle–bridge coupling analysis took into account the complex interactions among these components and employed the comfort index OVTV to assess how varying traffic densities, proportions, and road roughness impact driving comfort on the Yingwuzhou Bridge during vortex vibration events. Zhang et al. [26] developed a coupled eddy current–vehicle–bridge system tailored for addressing the multi-mode locking region observed in long-span suspension bridges. Adhering to ISO 2631-1 standards [14], the study examined the driving comfort index OVTV for three vehicles exposed to eddy vibrations and investigated wheel bouncing behavior that could occur in adverse road conditions and high-order eddy vibrations.

Previous research has predominantly concentrated on evaluating driving comfort using the OVTV index, while relatively limited attention has been given to the MSI index as outlined in ISO2631-1:1997 [14]. The novelty of this article lies in providing a convenient method for evaluating ride comfort under vortex-induced vibrations. The method offers the benefits of straightforward modeling and rapid calculations while avoiding complex finite element modeling and iterative solving. It can simply and quickly evaluate driving comfort after vortex-induced vibration occurs on a bridge. Simultaneously, it explores the MSI index, which has been overlooked by previous researchers, showcasing a new perspective for assessing ride comfort under vortex-induced vibrations, namely the MSI index. The objective of this study is to assess the ride comfort of vehicles encountering vertical bending vortex-induced vibrations on extended bridges. Vehicle models, accompanied by four-wheel road surface random excitation and wheel excitation input models during vortex-induced vibration, were developed to analyze the dynamic responses of individual vehicles under these conditions. This study investigates the impact of factors such as driving speed, vehicle type, vortex vibration frequency, vortex vibration amplitude, and road surface roughness on ride comfort, using both the OVTV index and the MSI index recommended by the ISO2631-1 standard [14]. Furthermore, it establishes a vortex-induced vibration limit based on ride comfort. The remaining sections of the paper are organized as follows: Section 2 describes the establishment of relevant models, Section 3 introduces the evaluation criteria for ride comfort, Section 4 presents the results of the case study and discusses the impact of key factors, and Section 5 provides the conclusion and comments on this study.

2. Modelling of Vehicle and Excitation under VIV

2.1. Modelling of Two-Axle Vehicle

Four typical vehicles, including a sedan car, a light truck, a minivan, and a motor bus, crossing a long-span bridge, are considered in this study. The above four vehicles are simplified and modeled as five rigid bodies connected by a series of dampers and springs, as shown in Figure 1.

This study primarily investigates the ride comfort of a single vehicle exposed to vertical bending vortex-induced vibrations on a long-span bridge. Considering that vortex-induced vibration usually occurs at low wind speeds, this paper does not consider the influence of crosswind on vehicles. Therefore, the two-axle vehicle model with five rigid bodies has a total of 15 degrees of freedom: the vertical, rolling, and pitching motion of the car body as well as the vertical motions of the four wheels. According to the structural dynamics principle, the dynamic equations of each vehicle are established, and then based on the literature [15,25,27], the appropriate parameters are selected. The equations of motion and vehicle parameters can be found in Appendix A. The method used to solve the equations is the unconditionally stable Newmark-beta method, where beta β is set to 0.5, and α is set to 0.25. The vehicle travels in a straight-line motion at a constant speed along the centerline of the bridge. The vehicle's gravity and dynamic response have a minimal impact on the long-span bridge when compared. Consequently, we have disregarded the interaction between the vehicle and the bridge, focusing solely on the one-way effect of the bridge on the vehicle.

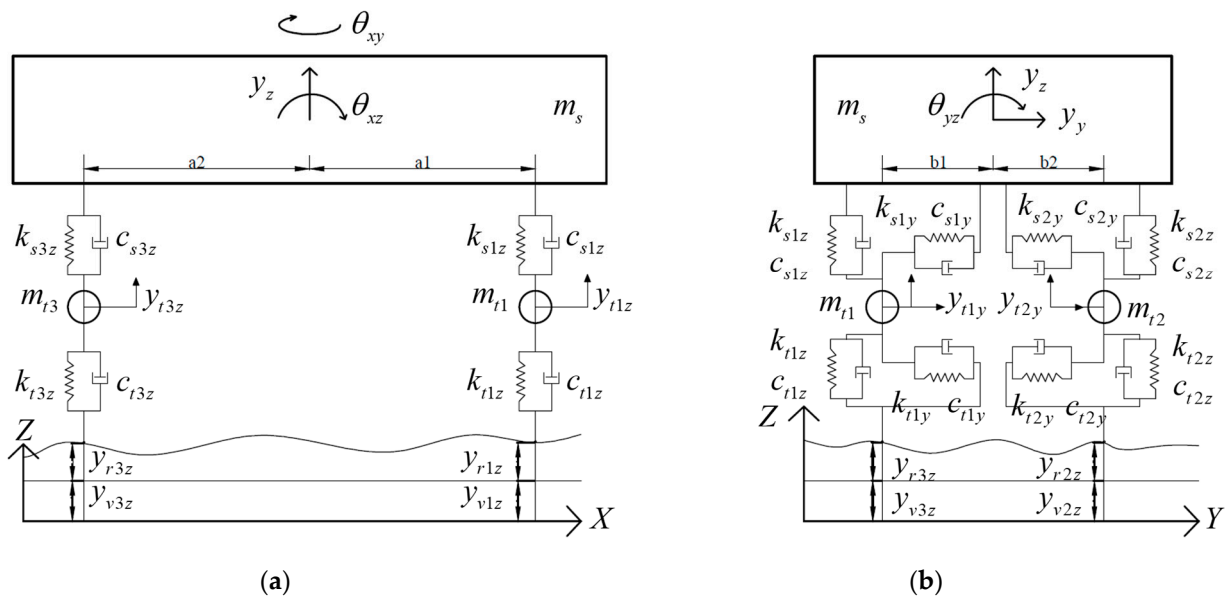


Figure 1. Model of the two-axle vehicle. (a) Elevation view. (b) Side view.

2.2. Four-Wheeled Road Excitation Model

Typically, road roughness is defined as the variation in height of the road surface with respect to a reference plane along the road’s length. It exhibits characteristics such as randomness, stability, ergodicity, and a zero mean value. This roughness is often modeled as a random process following a Gaussian probability distribution. In spectral analysis, the power spectrum with statistical characteristics is commonly employed. Currently, there are two methods for assessing road surface roughness. The first involves utilizing specialized instruments and continuous measurements to acquire the power spectral density of the road surface. However, this approach is labor-intensive and time-consuming. The second method relies on pre-existing power spectral density data of road surface roughness, which are commonly employed to simulate road surface unevenness.

According to ISO 8608 [28], the road surface power spectral density is fitted with the following formula:

$$G_q(n) = G_q(n_0) \left(\frac{n}{n_0} \right)^{-W}, \tag{1}$$

where $G_q(n_0)$ is unevenness index, which is classified into eight levels, from A to H; W is waviness; n is the spatial frequency, indicating the number of wavelengths contained in each meter of length; n_0 is the reference spatial frequency with a value of 0.1. Waviness $W = 2$ denotes the case when the change in the road vertical displacement per unit distance travelled is the frequency index, which indicates the frequency structure of the road surface power spectral density.

While the frequency index $W = 2$, the velocity power spectrum can be expressed as:

$$G_{\dot{q}}(n) = (2\pi n)^2 G_q(n_0) \left(\frac{n}{n_0} \right)^{-2} = (2\pi n_0)^2 G_q(n_0), \tag{2}$$

Equation (2) eliminates the spatial frequency; then, the speed power spectral density is only related to the road roughness coefficient but has nothing to do with frequency, which is the same as the white noise power spectrum characteristic. Therefore, the space velocity power spectrum can be simulated with white noise, or the displacement power spectrum can be simulated with integrated white noise, which is also the method used in this paper to construct the road roughness model.

The relationship between time frequency f , space frequency n , and vehicle speed v is as follows:

$$f = nv, \tag{3}$$

and, then, the relationship between time frequency bandwidth and corresponding space frequency bandwidth is:

$$\Delta f = \Delta n \cdot v, \tag{4}$$

and if the power spectral density is the “power” (mean square value) in the unit frequency band, then the spatial power spectral density is:

$$G_q(n) = \lim_{\Delta n \rightarrow 0} \frac{\sigma_{q \sim \Delta n}^2}{\Delta n}. \tag{5}$$

$\sigma_{q \sim \Delta n}^2$ is the power contained in the frequency band a of the road surface power spectral density. No matter how the speed changes, the power is always the same.

So, the time power spectrum and velocity power spectrum can be expressed as:

$$G_q(f) = \lim_{\Delta f \rightarrow 0} \frac{\sigma_{q \sim \Delta n}^2}{\Delta f} = \lim_{\Delta f \rightarrow 0} \frac{\sigma_{q \sim \Delta n}^2}{v \Delta n} = \frac{1}{v} G_q(n_0) \left(\frac{n}{n_0}\right)^{-2} = G_q(n_0) n_0^2 \frac{v}{f^2}, \tag{6}$$

$$G_q(f) = (2\pi f)^2 G_q(f) = 4\pi^2 G_q(n_0) n_0^2 v, \tag{7}$$

According to the random vibration theory, the road surface roughness model based on the filtered white noise method can be derived as follows:

$$G_q(\omega) = |H(j\omega)|^2 G_w(\omega), \tag{8}$$

where $G_q(\omega)$ is the displacement power spectrum of road surface roughness; $G_w(\omega) = G_w(f)/2\pi$ is the power spectrum of white noise; $G_w(f) = 1$.

$$G_q(\omega) = \frac{G_q(f)}{2\pi} = \frac{G_q(n_0) n_0^2 v}{2\pi \left(\frac{\omega}{2\pi}\right)^2} = \frac{2\pi G_q(n_0) n_0^2 v}{\omega^2}, \tag{9}$$

$$|H(j\omega)|^2 \frac{G_w(f)}{2\pi} \Big|_{G_w(f)=1} = \frac{2\pi G_q(n_0) n_0^2 v}{\omega^2}, \tag{10}$$

$$H(j\omega) = \frac{2\pi n_0 \sqrt{G_q(n_0) v}}{j\omega}, \tag{11}$$

$$\Delta f = \Delta n \cdot v H(s) = \frac{q(s)}{W(s)} = \frac{2\pi n_0 \sqrt{G_q(n_0) v}}{s}, \tag{12}$$

$$\dot{q}(t) = 2\pi n_0 \sqrt{G_q(n_0) v} w(t), \tag{13}$$

The ring space frequency corresponding to the cutoff frequency f_0 is n_{00} . Since the road surface spectrum is approximately horizontal in the low frequency range, the cutoff frequency f_0 can be introduced into the model:

$$G_q(f) = G_q(n_0) n_0^2 \frac{v}{(f + f_0)^2}, \tag{14}$$

Then, the frequency–response function is as follows:

$$H(j\omega) = \frac{2\pi n_0 \sqrt{G_q(n_0) v}}{j\omega + \omega_0}, \tag{15}$$

Finally, the road surface roughness model is obtained, which can be expressed as:

$$\dot{W}_1(t) = -2\pi n_{00}vW_1(t) + 2\pi n_{00}\sqrt{G_q(n_0)}vw(t), \tag{16}$$

where $w(t)$ denotes the white noise signal with a unilateral power spectral density of 1.

In order to verify the correctness of the model, the power spectrum of the generated road excitation curve of class A is compared with the power spectrum in the ISO standard. In the generated road excitation curve, the vehicle speed is 10 m/s, and the simulation time is 165 s, as shown in Figure 2.

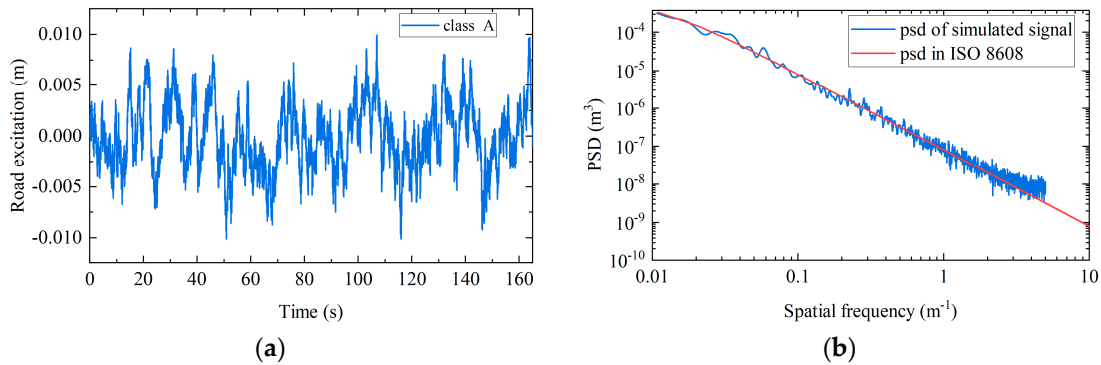


Figure 2. Single-wheel road excitation curve. (a) Time domain diagram of road excitation curve. (b) Frequency domain diagram of road excitation curve.

In Figure 2 and Table 1, the spectral density of the road random excitation generated through the simulation is basically consistent with the spectral density in the ISO 2631 standard [14], and the corresponding root mean square value is close. Thus, the road random excitation model obtained via simulation is reliable. In order to ensure that the time domain signal is not distorted, the sampling frequency should not be less than twice the maximum frequency of the road spectrum. The maximum spatial frequency of the standard spectrum is 10 m⁻¹, so the maximum spatial frequency of the simulated road spectrum is 5 m⁻¹.

Table 1. Comparison between simulated road model and standard road model.

Road Class	$G_q(n_0)/(10^{-6}m^3)$	$\sigma_{qsim}/(10^{-3}m)^1$	$\sigma_{qiso}/(10^{-3}m)^2$
A	16	3.60	3.81
B	64	7.10	7.61
C	256	14.30	15.23

¹ σ_{qsim} is the geometric mean of simulated road model. ² σ_{qiso} is geometric mean of road model in ISO 8608 [28].

To emulate genuine driving scenarios on the road and account for the spatiotemporal correlation amongst all four wheels, having previously established the single-wheel road random excitation model, it becomes essential to formulate a quad-wheel road random excitation model.

$$coh^2(\omega) = \frac{|G_{12}(\omega)|^2}{G_{12}(\omega)G_{22}(\omega)}, \tag{17}$$

where $G_{12}(\omega)$ and $G_{21}(\omega)$ represent the cross-spectrum between the left and right wheel tracks of the vehicle’s front axle; $coh(\omega)$ is the square root of the coherence function between the left and right wheel tracks. Equation (17) is predicated on the assumptions that the auto-power spectra of the car’s left and right wheel tracks are identical, the phase difference is zero, and the statistical properties are consistent.

The transfer function between the left and right wheel road surface white noise excitation inputs can be expressed as follows:

$$G_{21}(s) = \frac{W_2(s)}{W_1(s)} = \frac{a_0 + a_1s + a_2s^2 + \dots + a_ns^n}{b_0 + b_1s + b_2s^2 + \dots + b_ns^n} \tag{18}$$

$$|H(w)| = |G(jw)| = \left| \frac{a_0 + a_1(jw) + a_2(jw)^2 + \dots + a_n(jw)^n}{b_0 + b_1(jw) + b_2(jw)^2 + \dots + b_n(jw)^n} \right| \tag{19}$$

where W_1 and W_2 denote the left and right wheel road excitation inputs.

As for the coherence function $coh(\omega)$, it is the result of processing the driving signal collected by the CA141 vehicle on a certain asphalt road on the MTS road simulator of the Changchun Research Institute. The fitting expression of the coherence function is:

$$coh^2(f) = \begin{cases} 1 - 0.45f & f \leq 2Hz \\ 0.1 & f > 2Hz \end{cases} \tag{20}$$

Using optimization theory to solve the coefficients of the numerator and denominator of the transfer function, then Equation (18) can be simplified as follows:

$$G(s) = \frac{W_2(s)}{W_1(s)} = \frac{a_0 + a_1s + a_2s^2}{b_0 + b_1s + b_2s^2} = \frac{a_0s^{-2} + a_1s^{-1} + a_2}{b_0s^{-2} + b_1s^{-1} + b_2} \tag{21}$$

$$\begin{aligned} N(s) &= \frac{1}{b_2}W_1(s) - \frac{b_0}{b_2}s^{-2}N(s) - \frac{b_1}{b_2}s^{-1}N(s) \\ &= \frac{1}{a_2}W_1(s) - \frac{a_0}{a_2}s^{-2}N(s) - \frac{a_1}{a_2}s^{-1}N(s) \end{aligned} \tag{22}$$

Then, the state equation and output equation of left and right wheel road excitation can be obtained through the Laplace transform and inverse transform.

$$\begin{aligned} \dot{X}_1 &= \begin{bmatrix} -\frac{b_1}{b_2} & -\frac{b_0}{b_2} \\ 1 & 0 \end{bmatrix} X_1 + \begin{bmatrix} \frac{1}{b_2} \\ 0 \end{bmatrix} W_1 \\ W_2 &= \begin{bmatrix} (a_1 - a_2\frac{b_1}{b_2}) & (a_0 - a_2\frac{b_0}{b_2}) \end{bmatrix} X_1 + \frac{a_2}{b_2} W_1 \end{aligned} \tag{23}$$

Next, it is time to consider the correlation between front and rear wheel road excitation. The paper assumes that if the front and rear wheelbases of the vehicle are equal, and the vehicle is moving in a straight line at a constant speed, then the rear wheel input is the lag of the front wheel input for a period of time A , and then the road surface excitation of the front and rear wheels has the following relationship:

$$W_3(t) = W_1(t - t_d), \tag{24}$$

where $W_1(t)$ and $W_3(t)$ is the input of front and rear wheel road excitation, $t_d = L/v$, L is the wheelbase, and v is the speed of vehicle.

For pure time delay systems, we can use the Pade algorithm to approximate the calculation:

$$G_{31}(s) = \frac{W_3(s)}{W_1(s)} = \frac{1 - \frac{t_d}{2}s + P_2(t_d s)^2 - P_3(t_d s)^3 + \dots + (-1)^N P_N(t_d s)^N}{1 + \frac{t_d}{2}s + P_2(t_d s)^2 + P_3(t_d s)^3 + \dots + P_N(t_d s)^N} \tag{25}$$

The term N in Equation (25) is the order of the Pade algorithm; in this paper, $N = 2$ and $P = 1/12$.

$$G_{31}(s) = \frac{W_3(s)}{W_1(s)} = \frac{1 - \frac{t_d}{2}s + \frac{t_d^2}{12}s^2}{1 + \frac{t_d}{2}s + \frac{t_d^2}{12}s^2} \tag{26}$$

Drawing parallels to Equation (23), we obtain the state and output equations representing the correlation between the vehicle’s front and rear wheel tracks as follows:

$$\begin{aligned} \dot{X}_2 &= \begin{bmatrix} -\frac{6}{t_d} & -\frac{12}{t_d^2} \\ 1 & 0 \end{bmatrix} X_2 + \begin{bmatrix} \frac{12}{t_d^2} \\ 0 \end{bmatrix} W_1, \\ W_3 &= \begin{bmatrix} (1 - t_d/2) & 0 \end{bmatrix} X_2 + W_1 \end{aligned} \quad (27)$$

According to Equations (16), (23), and (27), the road surface excitation of the right front wheel, left front wheel, and right rear wheel can be calculated; then, the excitation of the left rear wheel can be expressed as follows:

$$\begin{aligned} W_4 &= \begin{bmatrix} (1 - t_d/2) & 0 \end{bmatrix} X_3 + \begin{bmatrix} (a_1 - a_2 \frac{b_1}{b_2}) & (a_0 - a_2 \frac{b_0}{b_2}) \end{bmatrix} X_1 + \frac{a_2}{b_2} W_1 \\ \dot{X}_3 &= \begin{bmatrix} -\frac{6}{t_d} & -\frac{12}{t_d^2} \\ 1 & 0 \end{bmatrix} X_3 + \begin{bmatrix} \frac{12}{t_d^2} \\ 0 \end{bmatrix} W_2; \quad \dot{X}_1 = \begin{bmatrix} -\frac{b_1}{b_2} & -\frac{b_0}{b_2} \\ 1 & 0 \end{bmatrix} X_1 + \begin{bmatrix} \frac{1}{b_2} \\ 0 \end{bmatrix} W_1 \end{aligned} \quad (28)$$

At this point, the four-wheel road excitation model has been established, taking a sedan car as an example, on a class A road with a speed of 36 km/h. The simulated four-wheel random road excitation curve is shown in Figure 3:

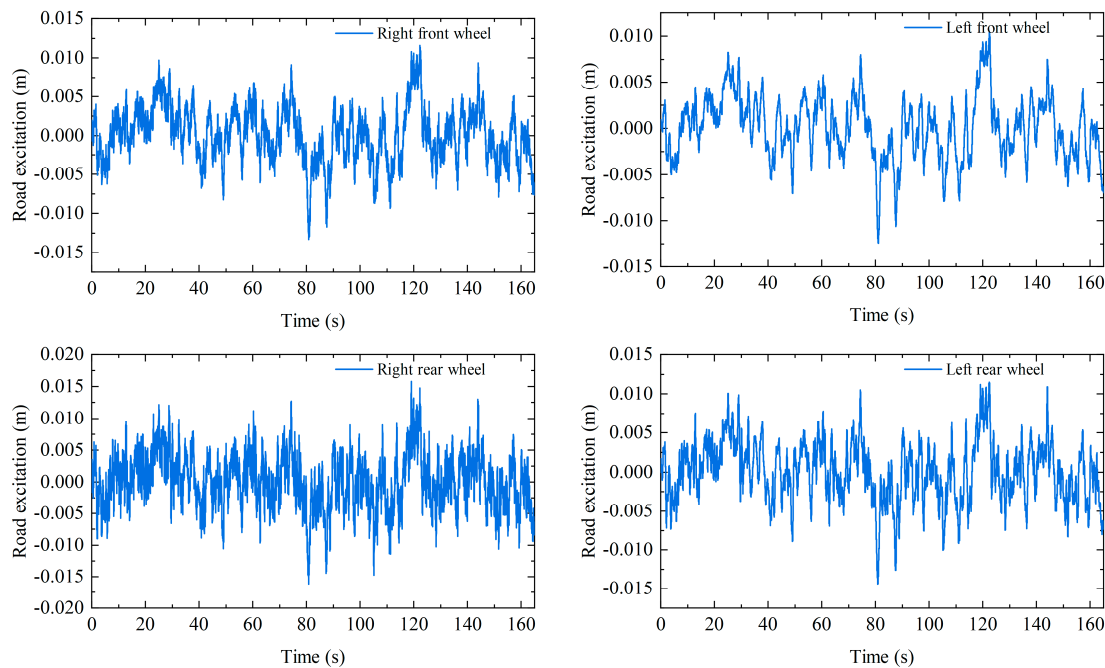


Figure 3. Four-wheel road excitation curve under A-class road surface.

This paper only considers the comfort of drivers and passengers when a single vehicle passes a long-span bridge under VIV, so this study ignores the interactions between the vehicle and the bridge.

2.3. Input Model of Wheel Excitation under Vortex Vibration of Main Beam

During the early exploration of vortex-induced vibration, researchers noticed that the observed vibrational behavior closely resembled that of simple harmonic motion. Consequently, they postulated that the forces exerted by vortex-induced phenomena on the structure exhibited characteristics akin to simple harmonic forces [29]. Therefore, for the purpose of this study, simple harmonic vibration will be employed to simulate the vibrational response at any given point along the bridge. Compared with the assumption of simple harmonic vibration, there are some enhanced methods [30] to calculate the VIV response with improved accuracy, including Scanlan’s model, the polynomial model, the

describing function-based model, Larsen's model and a newly developed aerodynamic envelope model. While these methods can enhance VIV amplitude calculation accuracy, they also decrease efficiency.

Simultaneously, this study assumes constant amplitude vortex vibration to investigate how frequency, amplitude, and other factors of vortex-induced vibration affect driving comfort. For constant amplitude and stable vortex-induced vibrations, aerodynamic forces exhibit harmonic stability. Therefore, simplifying constant amplitude vortex-induced vibrations into harmonic vibrations is feasible. This forms the basis for simplifying vortex-induced vibration as simple harmonic vibration in this article.

$$f(t) = A \sin(2\pi f_v \cdot t + \theta), \quad (29)$$

where A is the amplitude of vortex-induced vibration, f_v is the frequency of vortex vibration, and θ is the phase angle.

The vehicle travels in a straight-line motion at a constant speed along the centerline of the bridge, so the influence of torsional vortex-induced vibrations is minimal. In addition, based on the on-site monitoring data we measured, among the vortex-induced vibration events that have occurred, vertical bending vortex-induced vibrations are predominant, with very few instances of torsional vortex-induced vibrations. Therefore, the primary focus is on vertical bending vortex-induced vibrations, while neglecting torsional vortex-induced vibrations. When the vertical bending vortex-induced vibration with frequency A occurs on the main girder, the corresponding unit mode is S , and the vibration state at position x at time t on the bridge is:

$$y(x, t) = \psi(x) \cdot f(t), \quad (30)$$

In this study, if the vehicle moves in a straight line at a uniform speed, then the wheel excitation input is:

$$y(x, t) = \psi(vt) \cdot f(t), \quad (31)$$

Through utilizing Equation (31) as the input for the vortex vibration excitation of the front wheel of the vehicle, we can determine the input for the vortex vibration excitation of the rear wheel as follows:

$$y_B(x, t) = \psi\left(v\left(t - \frac{P}{v}\right)\right) \cdot f\left(\left(t - \frac{P}{v}\right)\right), \quad (32)$$

The bridge model's effect on the vehicle is transmitted through the simplified mass-spring-damper model representing the vehicle's wheels in this study. Consequently, this can be translated into inputs associated with wheel displacement and velocity excitations. We simplify the vortex-induced vibrations on the bridge as Equation (30). The bridge's impact on the vehicle is described by Equations (31) and (32). Furthermore, in the presence of constant amplitude and stable vortex-induced vibrations, the vortex causes little change the vibration characteristics of the bridge, including frequency and amplitude. The vortex's impact on the bridge is minimal; therefore, this study has neglected the effect of vortices.

Taking a certain bridge in China as a case study, we consider the presence of vortex-induced vibrations on the bridge with a frequency of 0.328 Hz and an amplitude of 0.1 m. The mode in Figure 4 is obtained through finite element calculation and verified with reference [28] to ensure the accuracy of the finite element calculation result. The gray color in the figure represents a simplified schematic diagram of the bridge without external forces, while the blue color represents the modal diagram of the bridge under vortex induced vibration. Furthermore, accounting for vehicle speeds of 10 m/s and 20 m/s, the wheel excitation input under vortex vibration is illustrated in Figure 5.

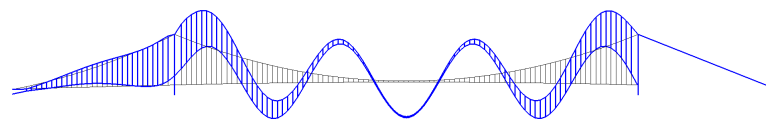


Figure 4. Vortex-induced vibration mode at 0.328 Hz [31].

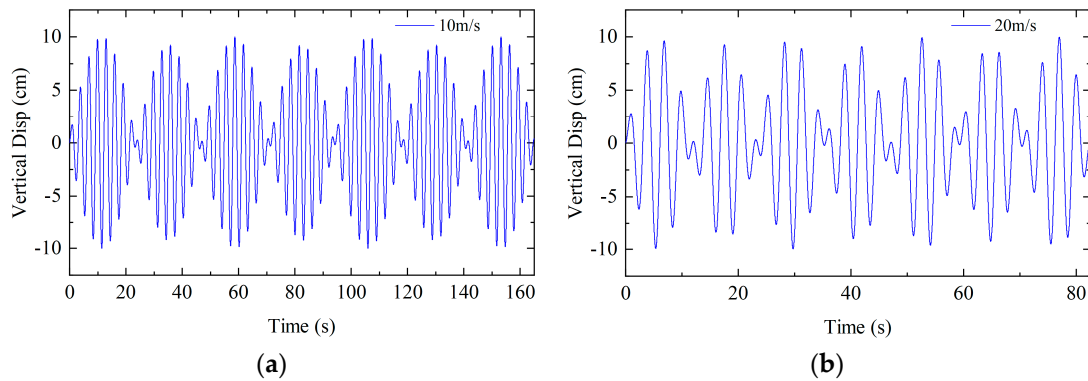


Figure 5. Vertical displacement of wheels under VIV. (a) Vehicle speed is 10 m/s. (b) Vehicle speed is 20 m/s.

3. Ride Comfort Criteria

According to the sources of discomfort, comfort can be categorized into six types: static, vibration, noise, heat, hearing pressure, and visual [32,33]. Generally, it is primarily assessed through collecting physiological data such as eye movement, EEG, and electrodermal activity, along with environmental vibration data in biological and medical fields [34,35]. Although this method can obtain relatively accurate results, it requires numerous personnel, extensive experimental equipment, and repeated experiments over extended periods, which is unsuitable for implementation in the field of engineering, owing to its time-consuming and labor-intensive nature. Currently, numerous objective evaluation methods exist globally for assessing ride comfort. These methods include the average absorbed power [36], VDI2057 [37], BS684:1987 [38], ISO2631-1 [14], Spurling stability index [39], UIC531 [40], EN12229:2009 [20], etc. Notably, the initial three methods find extensive application within the automotive industry, while the latter three are commonly employed in the railway industry. The ISO 2631-1 [14] standard serves as a universally applicable evaluation method. They provide comprehensive assessments that take into account factors such as resonance intensity, the human body's sensitive frequency range, and the applicable comfort index range. These methods primarily rely on frequency weighting functions for their calculations and evaluations. Among these approaches, the ISO2631-1 standard [14] evaluation method enjoys the broadest usage. Consequently, this paper utilizes the OTV and MSI indices from the ISO2631-1997 standard [14] to evaluate driving comfort, which mainly involves measuring physical attributes like frequency, amplitude, and the direction of a human body's vibrational response or the corresponding environmental vibrational response.

Methods for measuring periodic, random, and transient whole-body vibrations are defined in the ISO2631-1997 standard [14], considering three human vibration models of sitting, standing, and lying. In the evaluation of driving comfort in this paper, the sitting posture model is used. As shown in Figure 6, the vehicle vibration is mainly transmitted to the human body through the seat, backrest, and floor. In view of the complex modeling of the human body model, the vehicle vibration acceleration can be used to replace the vibration acceleration of each axis of the human body, which is used in some papers [24,25]. x_i, y_i, z_i ($i = b, s, f$) denote the line vibrations in three directions at the support surface, indicated by red arrows, where $i = b$ denotes the seat back support surface, $i = s$ denotes the seat support surface, and $i = f$ denotes the foot support surface. The blue dashed line indicates the reference system established through the seat support surface, mainly to

facilitate the representation of the 3 directions of rotation of the human body. The black arrows indicate the 3 directions of rotation, which is annotated in the Figure 6.

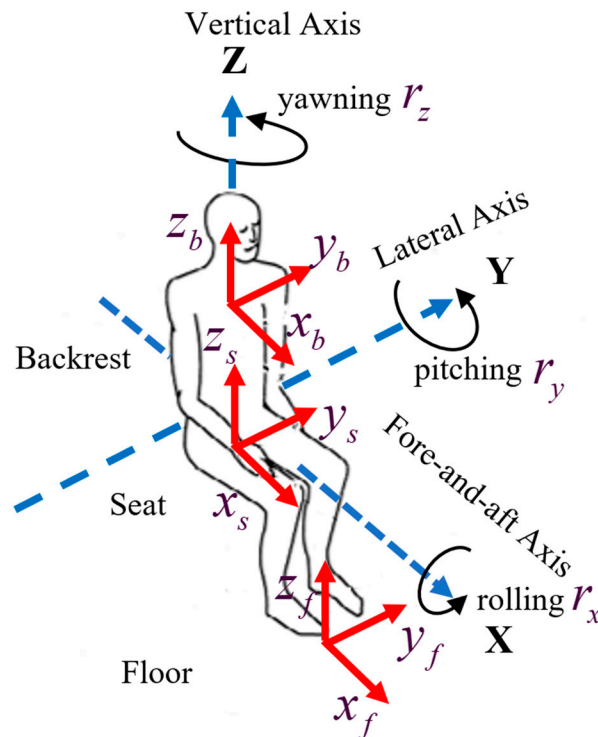


Figure 6. Vibration model for human sitting posture.

The vibration model for human sitting posture considers linear and angular vibrations in three directions at the seat surface input point. Additionally, it accounts for linear vibrations in three directions at both the seat backrest and foot support surface input points, resulting in a total of twelve axial vibrations across three input points. According to the ISO 2631-1997 standard [14], the human body exhibits varying sensitivities to vibrations at different frequencies. Frequency weighting functions are provided for each axis, as displayed in Figure 7. The axis weighting coefficients of each axial vibration are also specified in order to consider the differences in the impact of different input points and different axial vibrations on the human body.

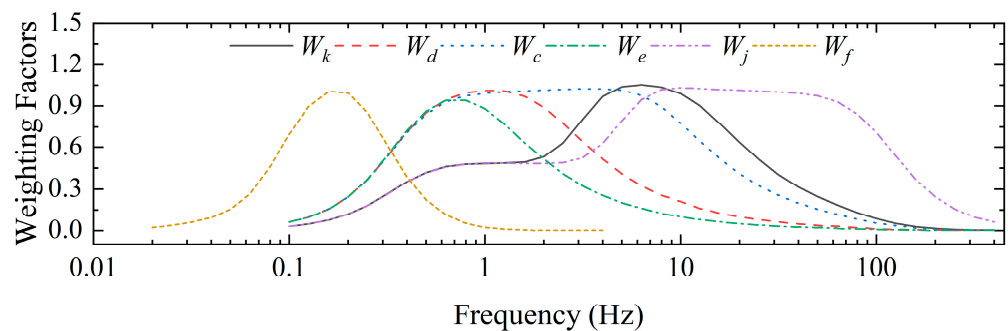


Figure 7. Weighting curve for different participating axes.

This paper mainly considers the influence of eight vibration accelerations on driving comfort under the sitting posture model: the vertical and lateral vibrations of the seat

surface, backrest, and floor and the pitch and roll of the seat position. The eight vibration accelerations can be converted from the vehicle acceleration:

$$\begin{aligned}
 a_{zb} &= a_{zs} = a_{zf} = \ddot{y}_z \\
 a_{yb} &= a_{ys} = a_{yf} = \ddot{y}_y \\
 a_{rx} &= \ddot{\theta}_{yz} \cdot y_s + \frac{1}{2} \ddot{\theta}_{yz} \cdot h_s \\
 a_{ry} &= \ddot{\theta}_{xz} \cdot d_s
 \end{aligned} \tag{33}$$

where a_{ij} indicates the vehicle acceleration; $i = z, y, r$; $j = b, s, f$. The subscripts z and y represent the vertical and horizontal directions, respectively, while the subscript r represents the direction of rotation, and the subscripts $b, s,$ and f represent the seat back, seat surface, and floor surface. $\ddot{y}_z, \ddot{y}_y, \ddot{\theta}_{yz}$, and $\ddot{\theta}_{xz}$ represent vertical, lateral, rolling, and pitching accelerations at the vehicle centroid; $d_s, y_s,$ and h_s are the longitudinal, transverse, and vertical distances between the vehicle centroid and the driver’s seat.

The ISO 2631-1 standard [14] uses the OVTV to evaluate vibrations ranging from 0.5 Hz to 80 Hz, while MSI assesses low-frequency vibrations below 0.5 Hz. Considering that vertical bending vortex vibrations in long-span bridges typically have frequencies below 0.5 Hz, it has been observed that drivers experience motion sickness and discomfort during vortex vibrations on the Humen Bridge. Consequently, this article incorporates the motion sickness index and analyzes the driving comfort of vortex vibrations considering both comfort and motion sickness. The calculation methods for the two indicators are as follows.

3.1. Calculation of Overall Vibration Total Value

Using the frequency weighting function provided in Table 2, each a_{ij} undergoes filtering to derive the time history signal $a_{\omega-ij}(t)$ representing the acceleration of human body vibrations. Subsequently, the second root mean square value (RMS_{ij}) of $a_{\omega-ij}(t)$ is calculated as follows:

$$RMS_{ij} = \left\{ \frac{1}{T} \int_0^T [a_{\omega-ij}(t)]^2 dt \right\}^{1/2}, \tag{34}$$

Table 2. Vibration component weighting function and axis weighting coefficient.

Location	Axis	Frequency Weighting Function	Axis Weighting Coefficients k
Seat	x_s	W_k	1.0
	y_s	W_d	1.0
	z_s	W_k	1.0
	r_x	W_e	0.20 m/rad
	r_y	W_e	0.40 m/rad
	r_z	W_e	0.63 m/rad
Backrest	x_b	W_c	0.8
	y_b	W_d	0.5
	z_b	W_d	0.4
Floor	x_f	W_k	0.25
	y_f	W_k	0.25
	z_f	W_k	0.4

Then, the axis weighting coefficients of the vibration components in each direction are combined using a weighted summation to calculate the Overall Vibration Total Value (OVTV), which represents the root mean square value of the total weighted acceleration.

$$OVTV = \left\{ \sum (M_{ij}RMS_{ij})^2 \right\}^{1/2}, \tag{35}$$

After the *OVTV* is calculated through Equation (35), the drivers’ ride comfort is assessed according to the criteria of different discomfort levels in Table 3 as recommended by ISO 2631-1 [14].

Table 3. Comfort criteria based on *OVTV* value.

<i>OVTV</i> (m/s ²)	Comfort Level
<0.315	Not Uncomfortable
0.315–0.630	A little Uncomfortable
0.500–1.000	Fairly Uncomfortable
0.800–1.600	Uncomfortable
1.250–2.500	Very Uncomfortable
>2.000	Extremely Uncomfortable

3.2. Calculation of Motion Sickness Incidence

The primary factor influencing motion sickness is the acceleration experienced in three directions: vertical, nodding, and rolling. Consequently, when analyzing motion sickness for drivers in vehicles, the considered accelerations include a_{zs} , a_{zf} , a_{zb} , a_{rx} , and a_{ry} . Similarly to the calculation method for the *OVTV*, the ISO 2631-1 standard [14] employs a specific frequency weighting function (W_f) to account for the influence of varying vibration frequencies on human motion sickness. This function applies frequency modulation to the accelerations measured in the aforementioned five directions. According to the ISO 2631-1 standard [14], it assumes that different positions and directions exert an equivalent effect on human motion sickness. Hence, the weighting coefficient assigned to each axial vibration component is set at 1.

$$MSDV_{ij} = \left\{ \int_0^T [a_{w-ij}(t)]^2 dt \right\}^{1/2} = RMS_{ij} T^{1/2}, \tag{36}$$

$$MSDV_T = \left\{ \sum (MSDV_{ij})^2 \right\}^{1/2}, \tag{37}$$

where *MSDV* denotes the motion sickness dose value, and *MSDV_T* represents the total motion sickness dose value considering the contributions of different axial accelerations.

$$MSI(\%) = K_m MSDV_T, \tag{38}$$

where the subscript K_m represents a constant, and for a group consisting of adult males and females, the ISO 2631-1 standard [14] recommends using the value 1/3. It is important to note that the resulting *MSI* is expressed as a percentage. The limitation of *MSI* is that there is no clear comfort limit standard, and it can only be analyzed qualitatively.

Motion sickness depends on various factors, including driver tolerance, individual differences (such as gender and age), and the duration of vibration exposure. According to the ISO 2631-1 standard [14], individual sensitivity to low-frequency oscillations varies significantly, with women being more susceptible than men. Individuals are generally susceptible to motion sickness, but the incidence of symptoms decreases with age. Longer exposure to vibration increases the likelihood of experiencing motion sickness.

4. Result and Discussion

4.1. Synopsis of a Certain Bridge

In this section, the vehicle model and corresponding excitation under the VIV established in Section 2 and the ride comfort criteria introduced in Section 3 are applied to a certain long-span bridge in China. Based on the design data, the bridge model is created within finite element software to calculate and analyze the dynamic characteristics. The resulting relationship between the modal frequency and the vertical bending mode diagram is presented in Table 4.

Table 4. Frequencies of vertical modes of vibration of the bridge.

Frequency (Hz)	Mode	Frequency (Hz)	Mode
0.082		0.276	
0.103		0.328	
0.121		0.381	
0.178		0.496	
0.197		0.557	
0.233			

4.2. Drivers' Ride Comfort Evaluation

4.2.1. OVTV

Taking a sedan car as an example, assuming that the vortex vibration frequency is 0.328 Hz and the amplitude is 0.3 m, the comfort OVTVs under different road grades and vehicle speeds are calculated, as shown in Figure 8.

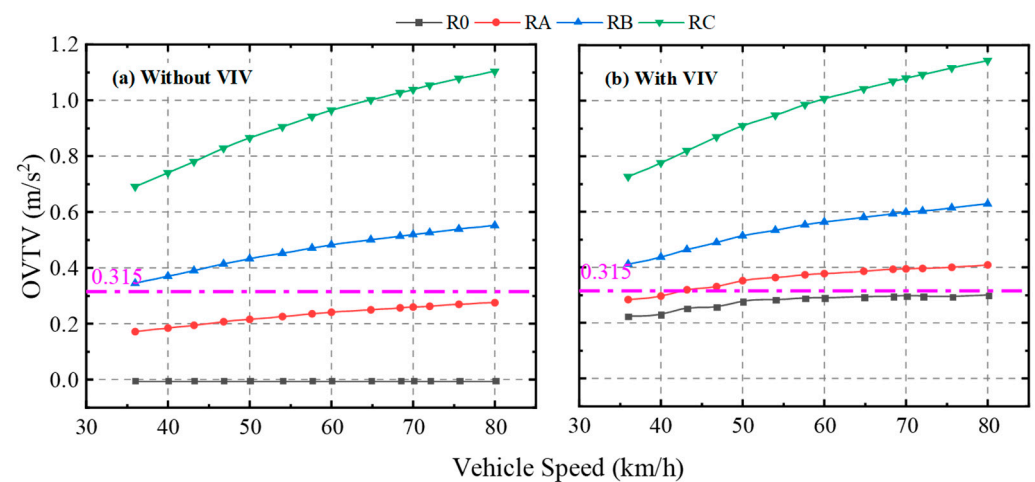


Figure 8. Relationship between OVTV and road grade and vehicle speed. (a) The comfort value of OVTV calculated without VIV (b) The comfort value of OVTV calculated with VIV.

In Figure 8, when the sedan car travels on a bridge without vortex-induced vibration, OVTVs for a Class A road are below 0.315 m/s², indicating that drivers experience no discomfort. Conversely, for Class B and C roads, OVTVs exceed 0.315 m/s², leading to considerable driver discomfort. However, when vertical bending vortex-induced vibrations occur in the main beam, irrespective of road surface roughness, OVTVs remain below 0.315 m/s², ensuring driver comfort. Notably, on A-class roads, vehicle speeds exceeding 45 km/h result in OVTVs surpassing 0.315 m/s², causing driver discomfort. This observation confirms that vortex-induced vibration does indeed lead to driving comfort issues. Generally, OVTVs increase with rising vehicle speed and road grade, indicating worsening comfort conditions as both parameters increase. Furthermore, when examining OVTVs under identical road conditions, with and without considering vortex-induced vibration (VIV), it becomes evident that the discrepancy between these two values is negligible. This suggests that the OVTV is not an appropriate metric for assessing driving comfort in the presence of vortex-induced vibration.

Figure 9 presents OVTVs for four vehicle types on a Class A road with the speed set at 80 km/h. The pink dashed line indicates the minimum comfort threshold, which is used to distinguish whether discomfort will be felt or not. It also illustrates their relationship with changes in vortex frequency and amplitude. When the amplitude ranges from 0.1 m to 0.5 m and the vortex vibration frequencies are below 0.276 Hz, comfort OVTVs remain below 0.315 m/s^2 , signifying driver comfort. However, starting at 0.276 Hz, the OVTV rapidly increases with amplified amplitude and frequency. Simultaneously, the comfort curves of the four vehicle types closely resemble each other, indicating minimal impact of the vehicle type on the OVTV. Overall, the comfort OVTV index rises with increasing vortex vibration amplitude and frequency. Notably, when the frequency ranges from 0.082 to 0.557 Hz and the amplitude remains below 0.1 m, the OVTV shows minimal variation, forming an almost linear trend.

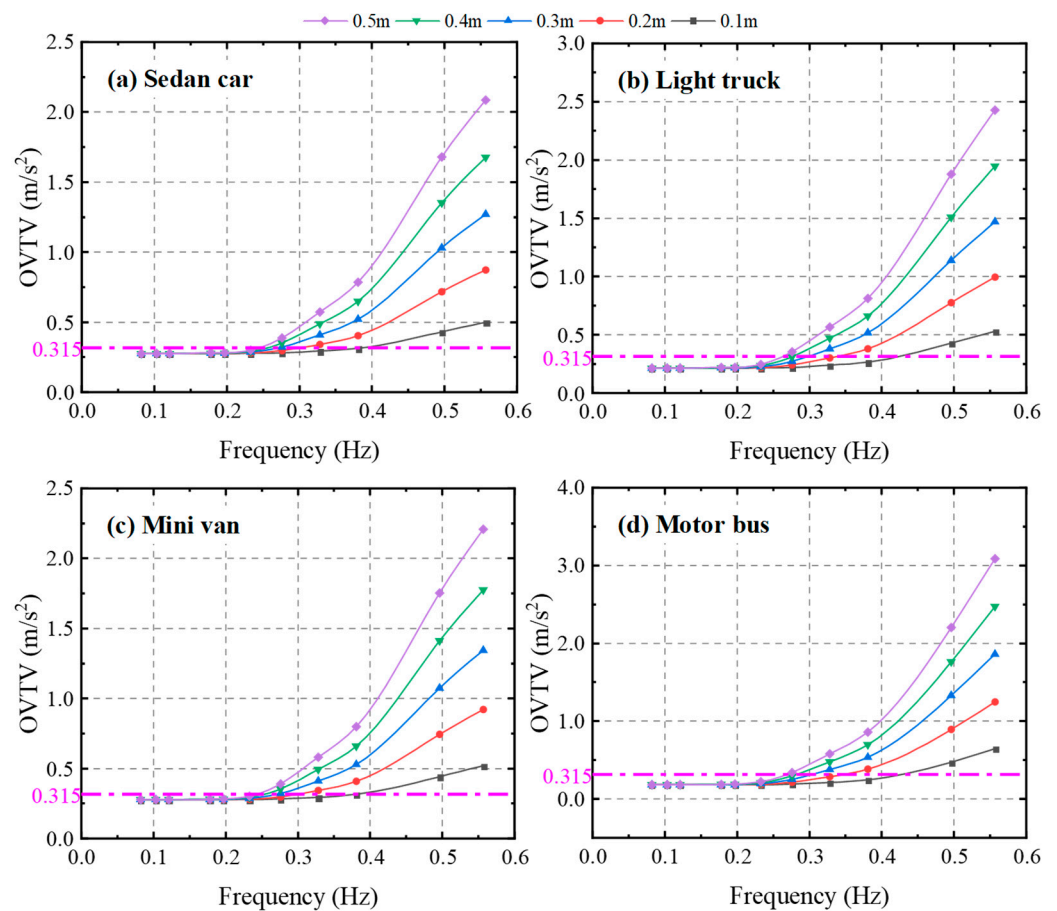


Figure 9. Relationship between OVTV and frequency and amplitude in different vehicles. (a) Sedan car (b) Light truck. (c) Mini van. (d) Motor bus.

It is important to highlight that within the 0.25 Hz range, the OVTV remains constant, regardless of vortex vibration frequency and amplitude. This stability arises because the frequency modulation coefficient corresponding to the frequency weighting function is nearly zero within this range. Consequently, the impact of vortex vibration excitation on the OVTV is minimal, while the acceleration response from the road surface dominates. However, when the frequency exceeds 0.25 Hz, the frequency modulation coefficient increases, resulting in a greater influence of eddy vibration-induced responses. Consequently, the OVTV starts to rise with higher vortex vibration frequencies and amplitudes.

4.2.2. MSI

Also taking a sedan car as an example, assuming that the vortex vibration frequency is 0.328 Hz and the amplitude is 0.3 m, the MSI values under different road grades and vehicle speeds are calculated, as shown in Figure 10.

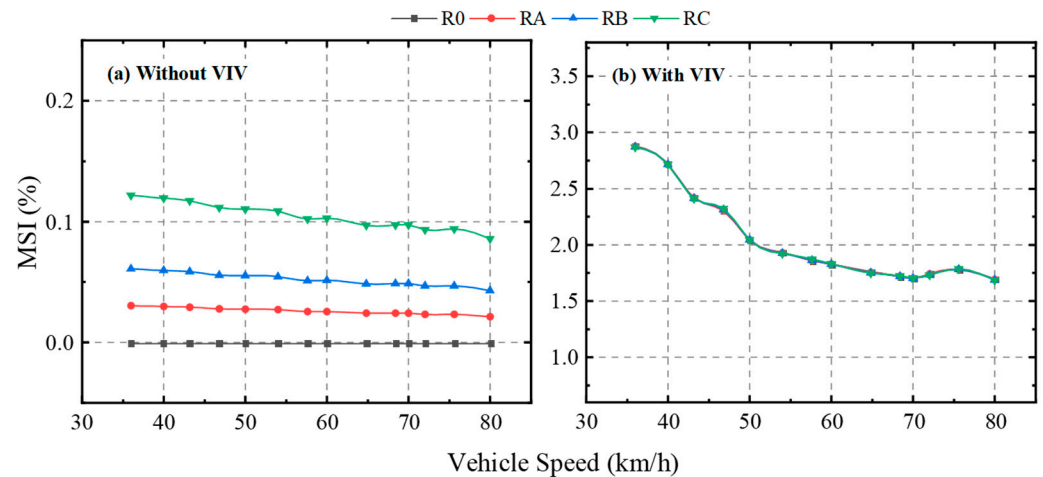


Figure 10. Relationship between MSI and road grade and vehicle speed. (a) The value of MSI calculated without VIV (b) The value of MSI calculated with VIV.

The Motion Sickness Index (MSI), expressed as a percentage, quantifies the morbidity of motion sickness in a given population. As depicted in the figure, the MSI decreases with higher vehicle speeds. This correlation arises from the inclusion of vibration duration in the MSI calculation, specifically, in relation to vehicle speed. Slower vehicle speeds result in an extended vibration duration, leading to higher MSI values and increased motion sickness incidence. Additionally, the MSI rises with heightened road roughness. In contrast to vortex vibration excitation, the MSI value under road excitation is negligible. Furthermore, when assessing MSI values under identical road surface conditions, with and without considering vortex-induced vibration (VIV), a significant disparity between these two values becomes apparent. This highlights that, in contrast to the OVTV, the MSI value is a more suitable metric for evaluating driving comfort in the presence of vortex-induced vibration.

As previously mentioned, the conditions in Figure 11 were configured with a vehicle speed of 40 km/h on a Class A road surface to investigate the MSI for four vehicle types. In the context of vortex vibration, there exists a relationship between the MSI value and vibration frequency and amplitude. Notably, the MSI value rises with increasing amplitude due to the amplified acceleration response associated with greater amplitudes. Furthermore, the MSI value exhibits an initial increase followed by a subsequent decrease as the frequency increases. This behavior can be attributed to the initial increase and subsequent decrease in the frequency modulation coefficient corresponding to the frequency weighting function W_f , occurring within the range of 0–0.5 Hz. Specifically concerning the MSI value, it reaches its peak when the bridge vortex vibration frequency falls within the range of 0.3–0.5 Hz. This indicates a relatively higher incidence of motion sickness among individuals exposed to high-order vortex vibration.

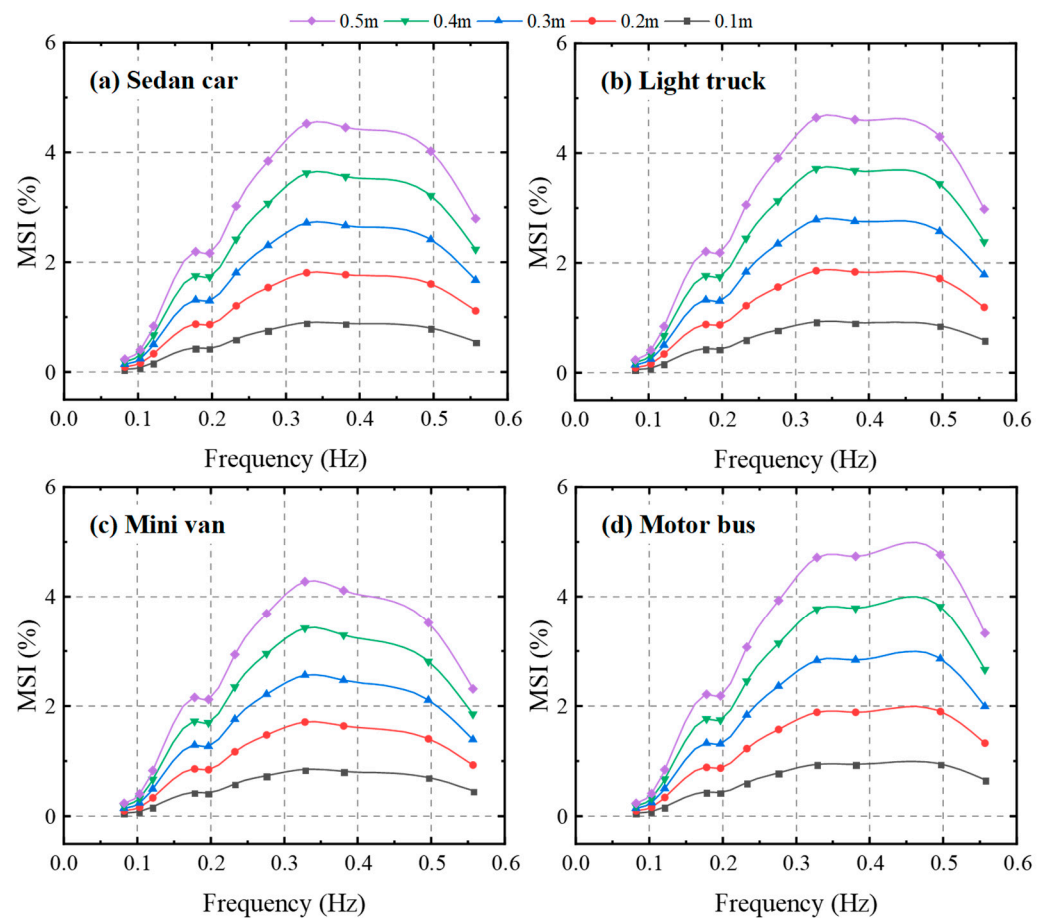


Figure 11. Relationship between MSI and frequency and amplitude in different vehicles. (a) Sedan car (b) Light truck. (c) Mini van. (d) Motor bus.

4.3. The Amplitude Limit of VIV Based on OVTV and MSI

During the initial phases of constructing long-span bridges, the bridge deck is built according to highway standards. Simultaneously, the bridge mentioned in Section 4.1 enforces a maximum speed limit of 80 km/h and a minimum speed limit of 40 km/h. Considering that higher vehicle speeds result in an increased OVTV and decreased MSI, we select an A-grade road surface and a vehicle speed of 80 km/h for calculating the comfort index OVTV under various frequency amplitude vortex vibrations. Based on the relationship between the OVTV and human subjective perception, we set a limit of 0.315 m/s^2 . After interpolation, we determined the driving comfort amplitudes for four vehicle types, which serve as the vortex-induced vibration limits. The results are presented in Table 5.

Table 5. Vortex-induced vibration limit based on OVTV (unit: m).

Frequency (Hz)	Sedan Car	Light Truck	Mini Van	Motor Bus
0.233	0.79	1.45	0.76	1.58
0.276	0.25	0.41	0.25	0.45
0.328	0.15	0.21	0.15	0.22
0.381	0.12	0.15	0.11	0.15
0.496	0.07	0.07	0.07	0.06
0.557	0.06	0.06	0.05	0.05

Similarly, we used interpolation to find corresponding amplitude values when MSI ranges from 1% to 10%. The minimum value for each vehicle type is set as its corresponding vortex-induced vibration limit based on MSI. These findings are shown in Table 6.

MSI values were calculated at a vehicle speed of 40 km/h. To provide a more intuitive representation of the results, Figure 12 have been added to illustrate how the amplitude limits vary with frequency.

Table 6. Vortex-induced vibration limit based on MSI (unit: m).

Frequency (Hz)	MSI (%)										
	1	2	3	4	5	6	7	8	9	10	
0.082	2.18	4.38	6.58	8.78	10.98	13.18	15.38	17.58	19.78	21.98	
0.103	1.22	2.45	3.67	4.90	6.12	7.35	8.58	9.80	11.03	12.25	
0.121	0.59	1.17	1.76	2.35	2.94	3.53	4.12	4.70	5.29	5.88	
0.178	0.22	0.44	0.66	0.88	1.10	1.32	1.54	1.76	1.98	2.21	
0.197	0.22	0.44	0.67	0.89	1.11	1.33	1.55	1.78	2.00	2.22	
0.233	0.16	0.31	0.47	0.62	0.78	0.94	1.09	1.25	1.41	1.56	
0.276	0.12	0.24	0.36	0.48	0.60	0.72	0.84	0.96	1.08	1.20	
0.328	0.10	0.19	0.29	0.39	0.49	0.58	0.68	0.78	0.87	0.97	
0.381	0.09	0.19	0.28	0.38	0.47	0.56	0.66	0.75	0.85	0.94	
0.496	0.09	0.17	0.26	0.34	0.43	0.51	0.60	0.68	0.77	0.86	
0.557	0.12	0.24	0.36	0.48	0.60	0.71	0.83	0.95	1.07	1.19	

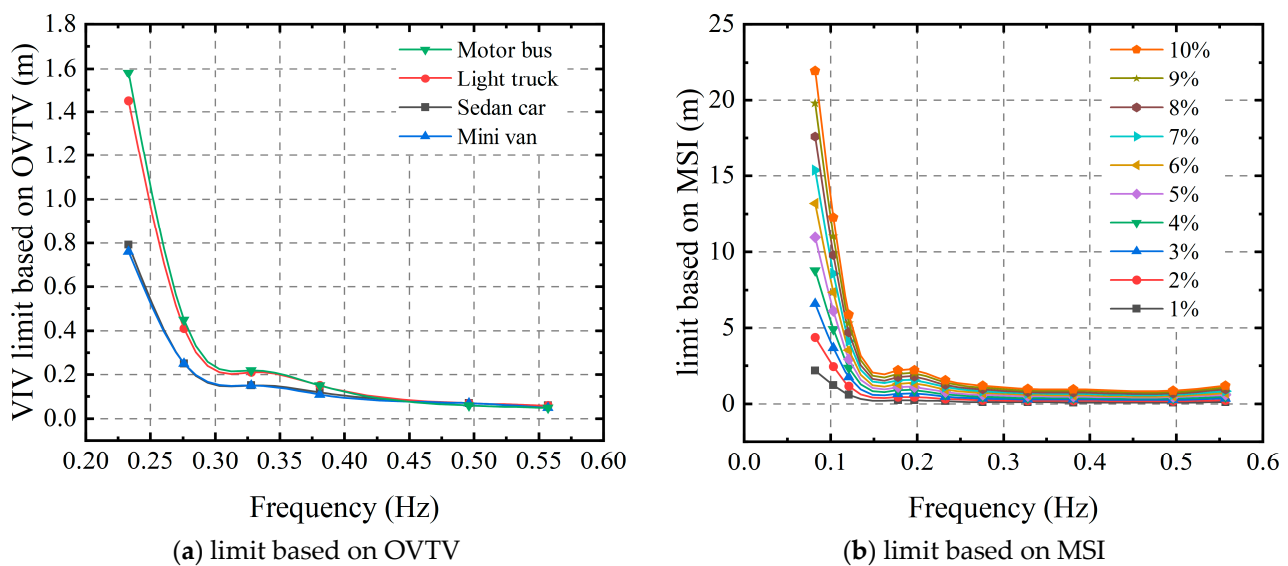


Figure 12. Vortex-induced vibration limit based on OVTV and MSI. (a) Vortex-induced vibration limit based on OVTV. (b) Vortex-induced vibration limit based on MSI.

5. Conclusions

This study introduces a road–bridge–vehicle vibration model and a rapid evaluation method to assess vehicle comfort during vortex-induced vibration on long-span bridges. The method offers the benefits of straightforward modeling and rapid calculations while avoiding complex finite element modeling and iterative solving. It can simply and quickly evaluate the driving comfort after vortex-induced vibration occurs on the bridge. The study analyses the impact of various parameters on the OVTV and MSI, including vehicle speed, road grade, vortex-induced vibration frequency, and amplitude. It establishes a reference limit value for vortex-induced vibration amplitude based on the OVTV and MSI values. Conclusions are drawn based on the study’s findings.

- Vortex-induced vibration significantly impacts driving comfort. Generally, as vehicle speed and road grade increase, the OVTV rises, suggesting a decline in comfort.

At vortex vibration frequencies below 0.276 Hz, the OVTV stays under 0.315 m/s², indicating no discomfort for drivers. However, beyond 0.276 Hz, OVTV increases rapidly with amplitude and frequency. Moreover, the comfort curves for all four vehicles are nearly identical, suggesting vehicle type has little impact on OVTVs.

- The MSI value increases with amplitude, a result of enhanced acceleration response. Additionally, as frequency rises, the MSI value initially increases but later decreases. This trend links to the frequency modulation coefficient associated with the frequency-weighting function W_f , which initially increases and then decreases within the range of 0–0.5 Hz. Importantly, the peak MSI value occurs within the 0.3–0.5 Hz vortex vibration frequency range. This suggests more motion sickness in individuals exposed to high-order vortex vibrations.
- Under the same road conditions, with or without considering VIV, OVTVs show minimal difference. However, MSI values vary significantly. This suggests that MSI is better suited than the OVTV to gauge driving comfort in the presence of vortex-induced vibrations.

Since vortex-induced vibrations mainly occur at low wind speeds, this study omits wind influence on vehicles. However, it is worth noting that some bridges often experience strong winds during high-order vortex-induced vibrations. Therefore, future research should investigate the impact of strong winds on driving comfort and safety under high-order VIVs. Additionally, it is important to mention that the Motion Sickness Incidence (MSI) index in the ISO 2631-1 standard [14] does not specify a comfort threshold. As a result, comfort evaluation on Motion Sickness Incidence currently relies on qualitative methods. Determining a quantitative comfort threshold for the MSI index remains an open research question.

Author Contributions: Conceptualization, Y.W., Z.W. and J.Z.; methodology, W.Y. and Y.J.; software, W.Y. and Y.J.; validation, Y.W., Z.W. and W.Y.; formal analysis, J.Z. and C.Z.; investigation, Y.J. and C.Z.; resources, Y.W. and S.L.; data curation, C.Z. and J.Z.; writing—original draft preparation, C.Z. and S.L.; writing—review and editing, S.L.; visualization, Y.W., Z.W. and J.Z.; supervision, S.L.; project administration, Y.W. and S.L.; funding acquisition, S.L. All authors have read and agreed to the published version of the manuscript.

Funding: This research was funded by the National Key Research and Development Program of China (2022YFC3005303), Open Projects Foundation (BHSKL20-01-KF) of the National Key Laboratory of Bridge Intelligent and Green Construction, National Natural Sciences Foundation of China (NSFC) (Grant No. 52178470), Natural Science Foundation of Heilongjiang Province under Grant No. YQ2021E033, Postdoctoral Scientific Research Development Fund of Heilongjiang Province under Grant No. LBH-Q20021, and Heilongjiang Touyan Team and Fundamental Research Funds for the Central Universities.

Institutional Review Board Statement: Not applicable.

Informed Consent Statement: Not applicable.

Data Availability Statement: The data presented in this study are available on request from the corresponding author.

Conflicts of Interest: The authors declare no conflict of interest.

Appendix A. Vehicle Dynamics Equations and Related Parameters

The equations of motion of a two-axle vehicle are as follows:

$$\begin{cases} x_{1z} = y_z - \theta_{xz}a_1 + \theta_{yz}b_1 \\ x_{2z} = y_z - \theta_{xz}a_1 - \theta_{yz}b_2 \\ x_{3z} = y_z + \theta_{xz}a_2 + \theta_{yz}b_1 \\ x_{4z} = y_z + \theta_{xz}a_2 - \theta_{yz}b_2 \end{cases} \begin{cases} x_{1y} = y_y - \theta_{xy}a_1 \\ x_{2y} = y_y - \theta_{xy}a_1 \\ x_{3y} = y_y + \theta_{xy}a_2 \\ x_{4y} = y_y + \theta_{xy}a_2 \end{cases} \quad (\text{A1a})$$

$$\begin{cases} x_{vz} = y_z - \theta_{xz}d_s - \theta_{yz}y_s \\ x_{2z} = y_y - \theta_{xy}d_s \end{cases} \tag{A1b}$$

$$\begin{aligned} & -a_1 [k_{s1z}(x_{1z} - y_{t1z}) + k_{s2z}(x_{2z} - y_{t2z}) + c_{s1z}(\dot{x}_{1z} - \dot{y}_{t1z}) + c_{s2z}(\dot{x}_{2z} - \dot{y}_{t2z})] \\ & + a_2 [k_{s3z}(x_{3z} - y_{t3z}) + k_{s4z}(x_{4z} - y_{t4z}) + c_{s3z}(\dot{x}_{3z} - \dot{y}_{t3z}) + c_{s4z}(\dot{x}_{4z} - \dot{y}_{t4z})] \\ & - d_s [k_{vz}(x_{vz} - y_{vz}) + c_{vz}(\dot{x}_{vz} - \dot{y}_{vz})] + J_{xz}\ddot{\theta}_{xz} = 0 \end{aligned} \tag{A1c}$$

$$\begin{aligned} & -b_2 [k_{s2z}(x_{2z} - y_{t2z}) + k_{s4z}(x_{4z} - y_{t4z}) + c_{s2z}(\dot{x}_{2z} - \dot{y}_{t2z}) + c_{s4z}(\dot{x}_{4z} - \dot{y}_{t4z})] \\ & + b_1 [k_{s1z}(x_{1z} - y_{t1z}) + k_{s3z}(x_{3z} - y_{t3z}) + c_{s1z}(\dot{x}_{1z} - \dot{y}_{t1z}) + c_{s3z}(\dot{x}_{3z} - \dot{y}_{t3z})] \\ & - y_s [k_{vz}(x_{vz} - y_{vz}) + c_{vz}(\dot{x}_{vz} - \dot{y}_{vz})] + J_{yz}\ddot{\theta}_{yz} = 0 \end{aligned} \tag{A1d}$$

$$\begin{aligned} & -a_1 [k_{s1y}(x_{1y} - y_{t1y}) + k_{s2y}(x_{2y} - y_{t2y}) + c_{s1y}(\dot{x}_{1y} - \dot{y}_{t1y}) + c_{s2y}(\dot{x}_{2y} - \dot{y}_{t2y})] \\ & + a_2 [k_{s3y}(x_{3y} - y_{t3y}) + k_{s4y}(x_{4y} - y_{t4y}) + c_{s3y}(\dot{x}_{3y} - \dot{y}_{t3y}) + c_{s4y}(\dot{x}_{4y} - \dot{y}_{t4y})] \\ & - d_s [k_{vy}(x_{vy} - y_{vy}) + c_{vy}(\dot{x}_{vy} - \dot{y}_{vy})] + J_{xy}\ddot{\theta}_{xy} = 0 \end{aligned} \tag{A1e}$$

$$m_s\ddot{y}_y + k_{s1y}(x_{1y} - y_{t1y}) + k_{s2y}(x_{2y} - y_{t2y}) + k_{s3y}(x_{3y} - y_{t3y}) + k_{s4y}(x_{4y} - y_{t4y}) + c_{s1y}(\dot{x}_{1y} - \dot{y}_{t1y}) + c_{s2y}(\dot{x}_{2y} - \dot{y}_{t2y}) + c_{s3y}(\dot{x}_{3y} - \dot{y}_{t3y}) + c_{s4y}(\dot{x}_{4y} - \dot{y}_{t4y}) = 0 \tag{A1f}$$

$$m_s\ddot{y}_z + k_{s1z}(x_{1z} - y_{t1z}) + k_{s2z}(x_{2z} - y_{t2z}) + k_{s3z}(x_{3z} - y_{t3z}) + k_{s4z}(x_{4z} - y_{t4z}) + c_{s1z}(\dot{x}_{1z} - \dot{y}_{t1z}) + c_{s2z}(\dot{x}_{2z} - \dot{y}_{t2z}) + c_{s3z}(\dot{x}_{3z} - \dot{y}_{t3z}) + c_{s4z}(\dot{x}_{4z} - \dot{y}_{t4z}) = 0 \tag{A1g}$$

$$m_s\ddot{y}_{t1y} + k_{t1y}(y_{t1y} - q_{1y}) + c_{t1y}(\dot{y}_{t1y} - \dot{q}_{1y}) + k_{s1y}(y_{t1y} - x_{1y}) + c_{s1y}(\dot{y}_{t1y} - \dot{x}_{1y}) = 0 \tag{A1h}$$

$$m_s\ddot{y}_{t1z} + k_{t1z}(y_{t1z} - q_{1z}) + c_{t1z}(\dot{y}_{t1z} - \dot{q}_{1z}) + k_{s1z}(y_{t1z} - x_{1z}) + c_{s1z}(\dot{y}_{t1z} - \dot{x}_{1z}) = 0 \tag{A1i}$$

$$m_s\ddot{y}_{t2y} + k_{t2y}(y_{t2y} - q_{2y}) + c_{t2y}(\dot{y}_{t2y} - \dot{q}_{2y}) + k_{s2y}(y_{t2y} - x_{2y}) + c_{s2y}(\dot{y}_{t2y} - \dot{x}_{2y}) = 0 \tag{A1j}$$

$$m_s\ddot{y}_{t2z} + k_{t2z}(y_{t2z} - q_{2z}) + c_{t2z}(\dot{y}_{t2z} - \dot{q}_{2z}) + k_{s2z}(y_{t2z} - x_{2z}) + c_{s2z}(\dot{y}_{t2z} - \dot{x}_{2z}) = 0 \tag{A1k}$$

$$m_s\ddot{y}_{t3y} + k_{t3y}(y_{t3y} - q_{3y}) + c_{t3y}(\dot{y}_{t3y} - \dot{q}_{3y}) + k_{s3y}(y_{t3y} - x_{3y}) + c_{s3y}(\dot{y}_{t3y} - \dot{x}_{3y}) = 0 \tag{A1l}$$

$$m_s\ddot{y}_{t3z} + k_{t3z}(y_{t3z} - q_{3z}) + c_{t3z}(\dot{y}_{t3z} - \dot{q}_{3z}) + k_{s3z}(y_{t3z} - x_{3z}) + c_{s3z}(\dot{y}_{t3z} - \dot{x}_{3z}) = 0 \tag{A1m}$$

$$m_s\ddot{y}_{t4y} + k_{t4y}(y_{t4y} - q_{4y}) + c_{t4y}(\dot{y}_{t4y} - \dot{q}_{4y}) + k_{s4y}(y_{t4y} - x_{4y}) + c_{s4y}(\dot{y}_{t4y} - \dot{x}_{4y}) = 0 \tag{A1n}$$

$$m_s\ddot{y}_{t4z} + k_{t4z}(y_{t4z} - q_{4z}) + c_{t4z}(\dot{y}_{t4z} - \dot{q}_{4z}) + k_{s4z}(y_{t4z} - x_{4z}) + c_{s4z}(\dot{y}_{t4z} - \dot{x}_{4z}) = 0 \tag{A1o}$$

The equations of motion can be summarized as follows:

$$[M]\{\ddot{y}\} + [C]\{\dot{y}\} + [K]\{y\} = \{F\} \tag{A2}$$

The variables in Equation (40) can be listed as follows:

$$\{y\} = \{\theta_{xz} \ \theta_{yz} \ \theta_{xy} \ y_y \ y_z \ y_{t1y} \ y_{t1z} \ y_{t2y} \ y_{t2z} \ y_{t3y} \ y_{t3z} \ y_{t4y} \ y_{t4z}\}^T \tag{A3a}$$

$$[M] = \text{diag}[J_{xz} \ J_{yz} \ J_{xy} \ m_s \ m_s \ m_{t1} \ m_{t1} \ m_{t2} \ m_{t2} \ m_{t3} \ m_{t3} \ m_{t4} \ m_{t4}] \tag{A3b}$$

$$[C] = \begin{bmatrix} [C_s]_{5 \times 5} & [C_{st}]_{5 \times 8} \\ [C_{ts}]_{8 \times 5} & [C_t]_{8 \times 8} \end{bmatrix}_{13 \times 13}, \quad [K] = \begin{bmatrix} [K_s]_{5 \times 5} & [K_{st}]_{5 \times 8} \\ [K_{ts}]_{8 \times 5} & [K_t]_{8 \times 8} \end{bmatrix}_{13 \times 13} \quad (A3c)$$

$$[C_s] = \begin{bmatrix} (c_{s1z} + c_{s2z})a_1^2 + (c_{s3z} + c_{s4z})a_2^2 & 0 & 0 & 0 & 0 & (c_{s3z} + c_{s4z})a_2 - (c_{s1z} + c_{s2z})a_1 \\ 0 & (c_{s1z} + c_{s3z})b_1^2 + (c_{s2z} + c_{s4z})b_2^2 & 0 & 0 & 0 & (c_{s1z} + c_{s3z})b_1 - (c_{s2z} + c_{s4z})b_2 \\ 0 & 0 & (c_{s1y} + c_{s2y})a_1^2 + (c_{s3y} + c_{s4y})a_2^2 & (c_{s3y} + c_{s4y})a_2 - (c_{s1y} + c_{s2y})a_1 & 0 & 0 \\ 0 & 0 & (c_{s3y} + c_{s4y})a_2 - (c_{s1y} + c_{s2y})a_1 & c_{s1y} + c_{s2y} + c_{s3y} + c_{s4y} & 0 & 0 \\ (c_{s3z} + c_{s4z})a_2 - (c_{s1z} + c_{s2z})a_1 & (c_{s1z} + c_{s3z})b_1 - (c_{s2z} + c_{s4z})b_2 & 0 & 0 & 0 & c_{s1z} + c_{s2z} + c_{s3z} + c_{s4z} \end{bmatrix} \quad (A3d)$$

$$[C_{st}] = \begin{bmatrix} 0 & c_{s1z}a_1 & 0 & c_{s2z}a_1 & 0 & -c_{s3z}a_2 & 0 & -c_{s4z}a_2 \\ 0 & -c_{s1z}b_1 & 0 & c_{s2z}b_2 & 0 & -c_{s3z}b_1 & 0 & c_{s4z}b_2 \\ c_{s1y}a_1 & 0 & c_{s2y}a_1 & 0 & -c_{s3y}a_2 & 0 & -c_{s4y}a_2 & 0 \\ -c_{s1y} & 0 & -c_{s2y} & 0 & -c_{s3y} & 0 & -c_{s4y} & 0 \\ 0 & -c_{s1z} & 0 & -c_{s2z} & 0 & -c_{s3z} & 0 & -c_{s4z} \end{bmatrix} \quad (A3e)$$

$$[C_{ts}] = \begin{bmatrix} 0 & 0 & c_{s1y}a_1 & -c_{s1y} & 0 \\ c_{s1z}a_1 & -c_{s1z}b_1 & 0 & 0 & -c_{s1z} \\ 0 & 0 & c_{s2y}a_1 & -c_{s2y} & 0 \\ c_{s2z}a_1 & c_{s2z}b_2 & 0 & 0 & -c_{s2z} \\ 0 & 0 & -c_{s3y}a_2 & -c_{s3y} & 0 \\ -c_{s3z}a_2 & -c_{s3z}b_1 & 0 & 0 & -c_{s3z} \\ 0 & 0 & -c_{s4y}a_2 & -c_{s4y} & 0 \\ -c_{s4z}a_2 & c_{s4z}b_2 & 0 & 0 & -c_{s4z} \end{bmatrix} \quad (A3f)$$

$$[C_t] = \text{diag}[c_{s1y} + c_{t1y} \quad c_{s1z} + c_{t1z} \quad c_{s2y} + c_{t2y} \quad c_{s2z} + c_{t2z} \quad c_{s3y} + c_{t3y} \quad c_{s3z} + c_{t3z} \quad c_{s4y} + c_{t4y} \quad c_{s4z} + c_{t4z}] \quad (A3g)$$

$$[K_s] = \begin{bmatrix} (k_{s1z} + k_{s2z})a_1^2 + (k_{s3z} + k_{s4z})a_2^2 & 0 & 0 & 0 & 0 & (k_{s3z} + k_{s4z})a_2 - (k_{s1z} + k_{s2z})a_1 \\ 0 & (k_{s1z} + k_{s3z})b_1^2 + (k_{s2z} + k_{s4z})b_2^2 & 0 & 0 & 0 & (k_{s1z} + k_{s3z})b_1 - (k_{s2z} + k_{s4z})b_2 \\ 0 & 0 & (k_{s1y} + k_{s2y})a_1^2 + (k_{s3y} + k_{s4y})a_2^2 & (k_{s3y} + k_{s4y})a_2 - (k_{s1y} + k_{s2y})a_1 & 0 & 0 \\ 0 & 0 & (k_{s3y} + k_{s4y})a_2 - (k_{s1y} + k_{s2y})a_1 & k_{s1y} + k_{s2y} + k_{s3y} + k_{s4y} & 0 & 0 \\ (k_{s3z} + k_{s4z})a_2 - (k_{s1z} + k_{s2z})a_1 & (k_{s1z} + k_{s3z})b_1 - (k_{s2z} + k_{s4z})b_2 & 0 & 0 & 0 & k_{s1z} + k_{s2z} + k_{s3z} + k_{s4z} \end{bmatrix} \quad (A3h)$$

$$[K_{st}] = \begin{bmatrix} 0 & k_{s1z}a_1 & 0 & k_{s2z}a_1 & 0 & -k_{s3z}a_2 & 0 & -k_{s4z}a_2 \\ 0 & -k_{s1z}b_1 & 0 & k_{s2z}b_2 & 0 & -k_{s3z}b_1 & 0 & k_{s4z}b_2 \\ k_{s1y}a_1 & 0 & k_{s2y}a_1 & 0 & -k_{s3y}a_2 & 0 & -k_{s4y}a_2 & 0 \\ -k_{s1y} & 0 & -k_{s2y} & 0 & -k_{s3y} & 0 & -k_{s4y} & 0 \\ 0 & -k_{s1z} & 0 & -k_{s2z} & 0 & -k_{s3z} & 0 & -k_{s4z} \end{bmatrix} \quad (A3i)$$

$$[K_{ts}] = \begin{bmatrix} 0 & 0 & k_{s1y}a_1 & -k_{s1y} & 0 \\ k_{s1z}a_1 & -k_{s1z}b_1 & 0 & 0 & -k_{s1z} \\ 0 & 0 & k_{s2y}a_1 & -k_{s2y} & 0 \\ k_{s2z}a_1 & k_{s2z}b_2 & 0 & 0 & -k_{s2z} \\ 0 & 0 & -k_{s3y}a_2 & -k_{s3y} & 0 \\ -k_{s3z}a_2 & -k_{s3z}b_1 & 0 & 0 & -k_{s3z} \\ 0 & 0 & -k_{s4y}a_2 & -k_{s4y} & 0 \\ -k_{s4z}a_2 & k_{s4z}b_2 & 0 & 0 & -k_{s4z} \end{bmatrix} \quad (A3j)$$

$$[K_t] = \text{diag}[k_{s1y} + k_{t1y} \quad k_{s1z} + k_{t1z} \quad k_{s2y} + k_{t2y} \quad k_{s2z} + k_{t2z} \quad k_{s3y} + k_{t3y} \quad k_{s3z} + k_{t3z} \quad k_{s4y} + k_{t4y} \quad k_{s4z} + k_{t4z}] \quad (A3k)$$

$$\{F\} = \begin{Bmatrix} 0_{5 \times 1} \\ k_{t1y}q_{1y} + c_{t1y}\dot{q}_{1y} \\ k_{t1z}q_{1z} + c_{t1z}\dot{q}_{1z} \\ k_{t2y}q_{2y} + c_{t2y}\dot{q}_{2y} \\ k_{t2z}q_{2z} + c_{t2z}\dot{q}_{2z} \\ k_{t3y}q_{3y} + c_{t3y}\dot{q}_{3y} \\ k_{t3z}q_{3z} + c_{t3z}\dot{q}_{3z} \\ k_{t4y}q_{4y} + c_{t4y}\dot{q}_{4y} \\ k_{t4z}q_{4z} + c_{t4z}\dot{q}_{4z} \end{Bmatrix} \tag{A3l}$$

$$\begin{cases} q_{1z} = y_{r1z} + y_{v1z} \\ q_{2z} = y_{r2z} + y_{v2z} \\ q_{3z} = y_{r3z} + y_{v3z} \\ q_{4z} = y_{r4z} + y_{v4z} \end{cases} \quad \begin{cases} q_{1y} = y_{r1y} + y_{v1y} \\ q_{2y} = y_{r2y} + y_{v2y} \\ q_{3y} = y_{r3y} + y_{v3y} \\ q_{4y} = y_{r4y} + y_{v4y} \end{cases} \tag{A3m}$$

where m_s is the mass of the vehicle body; m_{ti} ($i = 1; 2; 3; 4$) represents the total mass of the vehicle’s suspension devices and tires; k_{siy} and k_{siz} represent the lateral and vertical spring stiffness of the vehicle suspension system; k_{tiy} and k_{tiz} represent the lateral and vertical spring stiffness of the vehicle tires; c_{siy} and c_{siz} represent the lateral and vertical damping of the vehicle suspension system; c_{tiy} and c_{tiz} represent the lateral and vertical damping of the vehicle tires; θ_{xz} , θ_{yz} , and θ_{xy} represent the pitch angle, roll angle, and yaw angle of the vehicle body, respectively; y_y and y_z represent the lateral and vertical displacement of the vehicle body, respectively; y_{tiy} and y_{tiz} represent the lateral and vertical displacement of the wheel; i represents the i -th wheel ($i = 1, 2, 3, 4$). y_{riy} and y_{riz} represent the lateral and vertical excitation of the wheel when it is excited by road irregularities, and y_{viy} and y_{viz} represent the lateral and vertical excitation of the wheel when it is excited by the vibration of the bridge. a_1 and a_2 represent the distance from the front and rear axles to the center of gravity of the car, and b_1 and b_2 represent the lateral distances from the left and right wheels to the center of gravity of the vehicle.

The related parameters of vehicle are shown as Table A1. The selection of vehicle parameters refers to References [15,23,25].

Table A1. The related parameters of vehicles.

Parameter	Sedan Car	Light Truck	Mini Van	Motor Bus
m_s (kg)	1600	6500	6000	12,190
m_{t1}, m_{t2} (kg)	80	800	800	240
m_{t3}, m_{t4} (kg)	80	800	700	525
J_{xz} (kg/m ²)	2000	9550	34,000	79,000
J_{yz} (kg/m ²)	560	3030	2950	13,000
J_{xy} (kg/m ²)	32,000	100,000	12,500	53,000
k_{s1z}, k_{s2z} (kN/m)	50	250	200	126
k_{s3z}, k_{s4z} (kN/m)	50	250	225	225
c_{s1z}, c_{s2z} (kN·s/m)	6.229	2.5	3.85	9.15
c_{s3z}, c_{s4z} (kN·s/m)	2	2.5	2.72	18.3
k_{t1z}, k_{t2z} (kN/m)	192	175	363	750
k_{t3z}, k_{t4z} (kN/m)	192	175	422	1500
c_{t1z}, c_{t2z} (kN·s/m)	0.6	2.5	3	2
c_{t3z}, c_{t4z} (kN·s/m)	0.6	2.5	3	2
k_{s1y}, k_{s2y} (kN/m)	110	187.5	300	50
k_{s3y}, k_{s4y} (kN/m)	110	187.5	300	85
c_{s1y}, c_{s2y} (kN·s/m)	6.229	1	3.85	6
c_{s3y}, c_{s4y} (kN·s/m)	2	1	2.72	6

Table A1. Cont.

Parameter	Sedan Car	Light Truck	Mini Van	Motor Bus
k_{t1y}, k_{t2y} (kN/m)	110	100	120	300
k_{t3y}, k_{t4y} (kN/m)	110	100	120	600
c_{t1y}, c_{t2y} (kN·s/m)	0.6	1	3	2
c_{t3y}, c_{t4y} (kN·s/m)	0.6	1	3	2
a_1 (m)	1.4	1.8	3	1.8
a_2 (m)	1.7	2	2.6	3.4
b_1, b_2 (m)	0.72	1	0.75	0.9
h_s (m)	0.3	0.4	0.4	0.45
h_v (m)	0.72	1.65	1.5	1.35
d_s (m)	0.9	1.5	1.9	1.9
y_s (m)	0.9	0.4	0.4	0.4

References

- Zhu, J.; Zhang, W. Numerical Simulation of Wind and Wave Fields for Coastal Slender Bridges. *J. Bridge Eng.* **2017**, *22*, 04016125. [\[CrossRef\]](#)
- Battista, R.C.; Pfeil, M.S. Reduction of Vortex-Induced Oscillations of Rio–Niterói Bridge by Dynamic Control Devices. *J. Wind Eng. Ind. Aerodyn.* **2000**, *84*, 273–288. [\[CrossRef\]](#)
- Yang, Y.; Ma, T.; Ge, Y. Evaluation on Bridge Dynamic Properties and VIV Performance Based on Wind Tunnel Test and Field Measurement. *Wind Struct.* **2015**, *20*, 719–737. [\[CrossRef\]](#)
- Macdonald, J.H.G.; Irwin, P.A.; Fletcher, M.S. Vortex-Induced Vibrations of the Second Severn Crossing Cable-Stayed Bridge—Full-Scale and Wind Tunnel Measurements. *Proc. Inst. Civ. Eng.-Struct. Build.* **2002**, *152*, 123–134. [\[CrossRef\]](#)
- Frandsen, J.B. Simultaneous Pressures and Accelerations Measured Full-Scale on the Great Belt East Suspension Bridge. *J. Wind Eng. Ind. Aerodyn.* **2001**, *89*, 95–129. [\[CrossRef\]](#)
- Li, H.; Laima, S.; Ou, J.; Zhao, X.; Zhou, W.; Yu, Y.; Li, N.; Liu, Z. Investigation of Vortex-Induced Vibration of a Suspension Bridge with Two Separated Steel Box Girders Based on Field Measurements. *Eng. Struct.* **2011**, *33*, 1894–1907. [\[CrossRef\]](#)
- Fujino, Y.; Yoshida, Y. Wind-Induced Vibration and Control of Trans-Tokyo Bay Crossing Bridge. *J. Struct. Eng.* **2002**, *128*, 1012–1025. [\[CrossRef\]](#)
- Marra, A.M.; Mannini, C.; Bartoli, G. Van Der Pol-Type Equation for Modeling Vortex-Induced Oscillations of Bridge Decks. *J. Wind Eng. Ind. Aerodyn.* **2011**, *99*, 776–785. [\[CrossRef\]](#)
- Ge, Y.; Zhao, L.; Cao, J. Case Study of Vortex-Induced Vibration and Mitigation Mechanism for a Long-Span Suspension Bridge. *J. Wind Eng. Ind. Aerodyn.* **2022**, *220*, 104866. [\[CrossRef\]](#)
- Zhao, L.; Cui, W.; Shen, X.; Xu, S.; Ding, Y.; Ge, Y. A Fast On-Site Measure-Analyze-Suppress Response to Control Vortex-Induced-Vibration of a Long-Span Bridge. *Structures* **2022**, *35*, 192–201. [\[CrossRef\]](#)
- Zhao, L.; Liu, C.; Ge, Y. Vortex-Induced Vibration Sensitivity of Bridge Girder Structures (in Chinese). *Acta Aerodyn.* **2020**, *38*, 694–704. [\[CrossRef\]](#)
- Hwang, Y.C.; Kim, S.J.; Kim, H.K. Report of an Unexpected Vortex-Induced Vibration in an Actual Suspension Bridge. In *IABSE Conference: Structural Engineering: Providing Solutions to Global Challenges*; ISO: Geneva, Switzerland, 2015; pp. 832–835.
- Wu, T.; Kareem, A. An Overview of Vortex-Induced Vibration (VIV) of Bridge Decks. *Front. Struct. Civ. Eng.* **2012**, *6*, 335–347. [\[CrossRef\]](#)
- ISO 2631-1:1997; Mechanical Vibration and Shock—Evaluation of Human Exposure to Whole Body Vibration—Part 1: General Requirements. ISO: Geneva, Switzerland, 1997.
- Zhu, J.; Zhang, W.; Wu, M.X. Evaluation of Ride Comfort and Driving Safety for Moving Vehicles on Slender Coastal Bridges. *J. Vib. Acoust.* **2018**, *140*, 0510121–05101215. [\[CrossRef\]](#)
- Nguyen, K.; Camara, A.; Rio, O.; Sparowitz, L. Dynamic Effects of Turbulent Crosswind on the Serviceability State of Vibrations of a Slender Arch Bridge Including Wind-Vehicle-Bridge Interaction. *J. Bridge Eng.* **2017**, *22*, 06017005. [\[CrossRef\]](#)
- Camara, A.; Kavrakov, I.; Nguyen, K.; Morgenthal, G. Complete Framework of Wind-Vehicle-Bridge Interaction with Random Road Surfaces. *J. Sound Vib.* **2019**, *458*, 197–217. [\[CrossRef\]](#)
- Zhou, Y.; Chen, S. Vehicle Ride Comfort Analysis with Whole-Body Vibration on Long-Span Bridges Subjected to Crosswind. *J. Wind Eng. Ind. Aerodyn.* **2016**, *155*, 126–140. [\[CrossRef\]](#)
- Montenegro, P.; Ribeiro, D.; Ortega, M.; Millanes, F.; Goicolea, J.; Zhai, W.; Calçada, R. Impact of the Train-Track-Bridge System Characteristics in the Runnability of High-Speed Trains against Crosswinds-Part II: Riding Comfort. *J. Wind Eng. Ind. Aerodyn.* **2022**, *224*, 104987. [\[CrossRef\]](#)
- CEN; EN12299 Railway Applications—Ride Comfort for Passengers—Measurement and Evaluation. British Standard: London, UK, 2009.
- GB/T 5599-2019; Specification for Dynamic Performance Assessment and Testing Verification of Rolling Stock. Standardization Administration of the People's Republic of China: Beijing, China, 2019.

22. Bao, Y.; Zhai, W.; Cai, C.; Zhu, S.; Li, Y. Dynamic Interaction Analysis of Suspended Monorail Vehicle and Bridge Subject to Crosswinds. *Mech. Syst. Signal Process.* **2021**, *156*, 107707. [[CrossRef](#)]
23. Ribeiro, D.; Costa, B.; Cruz, L.; Oliveira, M.; Alves, V.; Montenegro, P.; Calcada, R. Simulation of the Dynamic Behavior of a Centenary Metallic Bridge under Metro Traffic Actions Based on Advanced Interaction Models. *Int. J. Struct. Stab. Dyn.* **2021**, *21*, 2150057. [[CrossRef](#)]
24. Yu, H.; Wang, B.; Zhang, G.; Li, Y.; Chen, X. Ride Comfort Assessment of Road Vehicle Running on Long-Span Bridge Subjected to Vortex-Induced Vibration. *Wind Struct.* **2020**, *31*, 393–402. [[CrossRef](#)]
25. Zhu, J.; Xiong, Z.; Yue, X.; Xu, H.; Li, Y. Ride Comfort Evaluation of Stochastic Traffic Flow Crossing Long-Span Suspension Bridge Experiencing Vortex-Induced Vibration. *J. Wind Eng. Ind. Aerodyn.* **2021**, *219*, 104794. [[CrossRef](#)]
26. Zhang, G.-Q.; Wang, B.; Zhu, Q.; Xu, Y.-L. Dynamic Behavior and Ride Comfort of a Vehicle Moving on a Long Suspension Bridge within Multi-Mode Lock-in Regions. *J. Wind Eng. Ind. Aerodyn.* **2023**, *234*, 105345. [[CrossRef](#)]
27. Chen, S.R.; Wu, J. Dynamic Performance Simulation of Long-Span Bridge under Combined Loads of Stochastic Traffic and Wind. *J. Bridge Eng.* **2010**, *15*, 219–230. [[CrossRef](#)]
28. *ISO 8608; Mechanical Vibration—Road Surface Profiles—Reporting of Measured Data.* International Standardization Organization: Geneva, Switzerland, 1995.
29. Chen, Z. *Bridge Wind Engineering*; China Communications Press: Beijing, China, 2005. (In Chinese)
30. Zhang, M.; Xu, F.; Øiseth, O. Aerodynamic Damping Models for Vortex-Induced Vibration of a Rectangular 4:1 Cylinder: Comparison of Modeling Schemes. *J. Wind Eng. Ind. Aerodyn.* **2020**, *205*, 104321. [[CrossRef](#)]
31. Li, H.; Laima, S.; Zhang, Q.; Li, N.; Liu, Z. Field Monitoring and Validation of Vortex-Induced Vibrations of a Long-Span Suspension Bridge. *J. Wind Eng. Ind. Aerodyn.* **2014**, *124*, 54–67. [[CrossRef](#)]
32. Mohammadi, A.; Amador-Jimenez, L.; Nasiri, F. A Multi-Criteria Assessment of the Passengers' Level of Comfort in Urban Railway Rolling Stock. *Sustain. Cities Soc.* **2020**, *53*, 101892. [[CrossRef](#)]
33. Ebe, K.; Griffin, M.J. Factors Affecting Static Seat Cushion Comfort. *Ergonomics* **2001**, *44*, 901–921. [[CrossRef](#)]
34. Kitajima, N.; Sugita-Kitajima, A. Ocular Counter-Rolling in Scuba Divers with Motion Sickness. *Auris. Nasus. Larynx* **2021**, *48*, 214–220. [[CrossRef](#)]
35. Lucas, G.; Kemeny, A.; Paillot, D.; Colombet, F. A Simulation Sickness Study on a Driving Simulator Equipped with a Vibration Platform. *Transp. Res. Part F Traffic Psychol. Behav.* **2020**, *68*, 15–22. [[CrossRef](#)]
36. Pradko, F.; Lee, R.A. *Vibration Comfort Criteria*; SAE International: Warrendale, PA, USA, 1966.
37. Hohl, G.H. Ride Comfort of Off-Road Vehicles. In Proceedings of the International Conference on the Performance of Off-Road Vehicles and Machines (8th), Cambridge, UK, 5–11 August 1984; pp. 413–432.
38. *Guide B S BS 6841; Measurement and Evaluation of Human Exposure to Whole-Body Mechanical Vibration and Repeated Shock.* British Standards Institution: London UK, 1987.
39. Sperling, E.; Betzhold, C. Beitrag Zur Beurteilung Des Fahrkomforts in Schienenfahrzeugen. *Glas. Ann.* **1956**, *80*, 314–320.
40. *Leaflet U I C 513R; Guidelines for Evaluating Passenger Comfort in Relation to Vibration in Railway Vehicle.* International Union of Railways: Paris, France, 1994.

Disclaimer/Publisher's Note: The statements, opinions and data contained in all publications are solely those of the individual author(s) and contributor(s) and not of MDPI and/or the editor(s). MDPI and/or the editor(s) disclaim responsibility for any injury to people or property resulting from any ideas, methods, instructions or products referred to in the content.